ELSEVIER

Solid State Ionics 140 (2001) 161–171

SOLID STATE IONICS

www.elsevier.com/locate/ssi

Grain-sized influence on the phase transition of $Bi_{26}Mo_9WO_{69}$: an X-ray diffraction and impedance spectroscopy study

F.C. Fonseca [a], M.C. Steil [b,*], R.N. Vannier [b], G. Mairesse [b], R. Muccillo [a]

[a] *Instituto de Pesquisas Energéticas e Nucleares, Comissão Nacional de Energia Nuclear, C.P. 11049, Pinheiros, 05422-970, Sao Paulo, SP, Brazil*

[b] *Laboratoire de Cristallochimie et Physicochimie du Solide (UPRES A 8012), ENSCL, BP 108, 59652 Villeneuve d'Ascq cedex, France*

Received 24 July 2000; received in revised form 6 November 2000; accepted 22 January 2001

Abstract

In order to investigate the microstructure dependence of the monoclinic–triclinic phase transition of $Bi_{26}Mo_9WO_{69}$, dense samples with different grain sizes were produced by isostatic pressing and controlling sintering temperature and time. The structural and electrical properties were studied by X-ray diffraction (at room and at high temperature) and impedance spectroscopy, respectively. The influence of the microstructural properties on the triclinic–monoclinic phase transition and on the electrical properties of the $Bi_{26}Mo_9WO_{69}$ were described by the following parameters derived from the fitting of impedance diagrams: depression angle, relaxation frequency and total electrical conductivity. Impedance spectroscopy results are in agreement with the high-temperature X-ray diffraction data; both techniques show that phase transition kinetics depends on the microstructural properties, remarkably on the grain size.

Keywords: Oxide ion conductor; Microstructure; Phase transition; Electrical properties

1. Introduction

In the field of oxide ion conduction, bismuth-based materials exhibit interesting electrical properties at moderate temperatures: 300–600°C. Depending on their dimensionality, they can be classified into three groups: three-dimensional ion conductors, Bi_2O_3 being the prototype of the bismuth-based oxides [1]; two-dimensional ion conductors represented by the BIMEVOX family, which has generated an increasing interest during the last decade [2]; one-dimensional ion conductors, with $Bi_{26}Mo_{10}O_{69}$ and related phases, with a structure based on $[Bi_{12}O_{14}]_\infty$ columns [3].

Depending on the temperature, $Bi_{26}Mo_{10}O_{69}$ exhibits two polymorphs: a triclinic form, stable from room temperature to 310°C, and a monoclinic one, stable above 310°C up to the melting point (~ 975°C). The triclinic distortion at room temperature is very small and the $Bi_{26}Mo_{10}O_{69}$ structure was resolved in $P_{2/c}$ space group with $a = 11.742$ (8) Å, $b = 5.800$ (7) Å, $c = 27.77$ (5) Å and $\beta =$

* Corresponding author. Tel.: +33-3-2043-4434; fax: +33-3-2043-6814.

E-mail addresses: cfonseca@net.ipen.br (F.C. Fonseca), c.steil@pop.ensc-lille.fr (M.C. Steil), muccillo@usp.br (R. Muccillo).

0167-2738/01/$ - see front matter
PII: S0167-2738(01)00705-6

102.94 (6)° from single crystal X-ray diffraction data [3]. In order to improve the electrical properties of this phase, several attempts of substitution for bismuth or molybdenum were performed [4]. The best properties were obtained for tungsten-doped phases. A $Bi_{26}Mo_{10-x}W_xO_{69}$ solid solution with $0 \leq x < 2$ was evidenced. At room temperature the symmetry of these phases remains triclinic within the entire solid solution domain, and a decrease of the temperature of phase transition is observed when the substitution ratio is increased. For $x = 1$, this phase transition temperature decreases to 250°C. An electrical conductivity value of 10^{-3} S cm^{-1} was measured at 350°C with a thermal activation energy of 0.43 eV in the monoclinic domain [4].

These materials are potentially attractive for use as electrolytes in some devices such as oxygen generators. For this application a compactness higher than 95% is required [5]. Therefore, to have usable dense ceramics, the sintering conditions have to be optimized.

The effect of grain size on phase transitions is well known. A typical example is the tetragonal–monoclinic phase transition in zirconia-based ceramics [6–8].

After the work by Bauerle [9], impedance spectroscopy has become an important technique to study electrical properties of materials, and today it is a standard technique for solid electrolyte characterization. Many efforts trying to correlate the electrical properties to the microstructural properties using impedance spectroscopy have been reported. Grain growth and pore elimination during sintering of yttria-stabilized zirconia [10–12], cubic phase decomposition of magnesia partially stabilized zirconia [13], dependence of the electrical properties on grain size of BICOVOX [14], characterization of highly conductive grain boundaries in AgCl [15] and the powder synthesis technique effect on the electrical conductivity of LSGM [16], are some examples of the use of this technique to study the dependence of the electrical properties of different materials on their microstructure.

In this study, the $Bi_{26}Mo_9WO_{69}$ composition was selected. In a first step, the sintering behavior was studied; in a second step, the influence of the microstructure on the phase transition and on the electrical properties was examined.

2. Experimental

2.1. Sample elaboration

$Bi_{26}Mo_9WO_{69}$ powder was prepared by solid state reaction in air from stoichiometric amounts of Bi_2O_3 (Riedel-De-Haën, 99.5% purity, previously decarbonated at 600°C), MoO_3 (Merck, 99.5%) and WO_3 (Riedel-De-Haën, 99%), as previously described [3].

The powder mixture was attrition milled (Netzsch PE 075) with zirconia balls (2 mm diameter) to reduce the mean particle size. The milling conditions were: 30 wt.% of $Bi_{26}Mo_9WO_{69}$ in a suspension of ethanol, 1000 rpm, for 4 h. After milling, the powder was dried for 20 h at 100°C and granulated with a 100 μm sieve. The resulting powder was analyzed by SEM and the estimated average particle size was smaller than 1 μm.

The sintering behavior was studied by dilatometric analysis (Linseis dilatometer) with 10°C/min heating rate, 900°C maximum temperature, 1 h holding time at maximum temperature and 10°C/min cooling rate in air.

Cylindrical pellets (10 mm diameter and approximately 4 mm thickness) were prepared by uniaxial pre-pressing followed by isostatic pressing at 150 MPa. The average green density was $57.3 \pm 0.7\%$ TD (theoretical density = 7.63 g/cm^3 [4]). A $Bi_{26}Mo_9WO_{69}$ powder bed inside an alumina crucible was used for sintering in a resistive furnace. In order to obtain different average grain sizes, sintering temperatures ranged from 750°C to 900°C and sintering time from 0.2 to 36 h. Heating and cooling rates were 10°C/min. Three supposedly identical samples of each different sintering temperature and time were produced for evaluation of experimental dispersion of density determinations. After sintering, samples were machined with SiC paper and cleaned with ethanol in ultrasound. Final typical dimensions were 7 mm diameter and 3 mm thick.

Polished and thermally etched samples were observed in a Jeol JSM5300 scanning electron microscope for microstructural characterization. Surfaces were polished with SiC paper. Grain boundaries were revealed by thermal etching at 50°C (or 100°C depending on sintering temperature) below the sintering temperature for 20 min. For SEM observation,

polished surfaces were covered with gold by sputtering.

2.2. X-ray diffraction and impedance spectroscopy

Powder specimens were analyzed by X-ray diffraction (Siemens D5000 diffractometer) using Cu K_α radiation. For room temperature analysis, the measurements were performed in $\theta/2\theta$ scanning mode in the 5–60° 2θ range, with a 0.02° step size and 15 s counting time, using a graphite monochromator and a scintillation detector. For high-temperature experiments, a HTK 1200 Anton Paar device and a position-sensitive detector (PSD) were used. The analyses were performed in the 10–70° 2θ range in θ/θ scanning mode with a 0.015° step size and a 0.25 s counting time with a delay of 60 s (each diffractogram was recorded in about 18 min) between 40°C and 400°C with a temperature step of 20°C and a scanning rate of 0.1°C/s on heating and cooling.

The electrical properties were studied by impedance spectroscopy with a computer controlled Solartron 1260 impedance analyzer with 1 V amplitude signal over the 1 Hz to 30 MHz frequency range. A stainless steel sample holder, for three samples, with type K thermocouple and gold leads was used inside an alumina tube positioned in a resistive furnace. The alumina tube has its outer surface painted with platinum paste and is electrically shielded from the furnace by a conductive net connected to ground. Gold electrodes were applied to the parallel surfaces of the samples by sputtering. Impedance measurements were performed in three consecutive heatings between 200°C and 500°C in air. All impedance diagrams were normalized to a geometrical factor equal to one. The curve fitting was done with the ZView software (Scribner Associates).

3. Results and discussion

3.1. Sintering behavior and sample microstructure

Fig. 1 shows the dilatometric curve and its derivative for $Bi_{26}Mo_9WO_{69}$. The shrinkage starts at approximately 550°C and the maximum densification

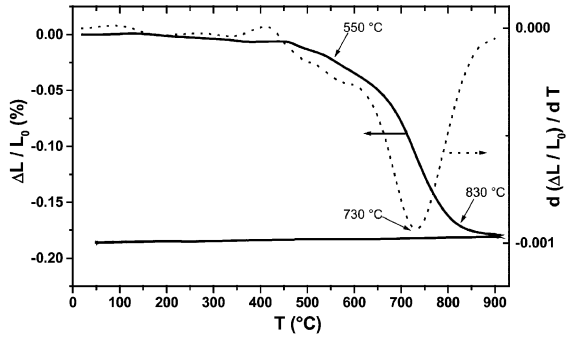

Fig. 1. Shrinkage curve and its derivative (dotted curve) as a function of temperature for $Bi_{26}Mo_9WO_{69}$.

temperature is 730°C. The sintering process finishes at about 830°C with a final shrinkage of approximately 17%.

Table 1 shows the relative densities of ceramic samples for different sintering temperatures and times. Samples sintered for 1 h at temperatures between 750°C and 900°C reach the maximum relative density values (around 96.5%). The sample sintered at 750°C/0.2 h has the lowest relative density (91.5%), probably related to incomplete pore elimination. Slightly lower relative densities are observed for samples sintered at 900°C for longer times (12 and 36 h).

Fig. 2 shows typical micrographs corresponding to samples sintered at 750°C/0.2 h, 750°C/1 h, 800°C/1 h, 850°C/1 h, 900°C/1 h and 900°C/36 h. A first observation shows that the specimens are dense with low intergranular porosity. An increase of grain size with increasing sintering temperature and time is noticed. The estimated average grain size for the sample sintered at 750°C/1 h is about 1 μm and for the sample sintered at 900°C/1 h is about 10 μm. Samples sintered at 750°C are more homogeneous than samples sintered at higher temperatures, which show abnormal grain growth. Cracks are evidenced for samples sintered at 900°C and their number and length increase with sintering time. The presence of cracks is a possible explanation for the slight decrease of relative density values for samples sintered at 900°C for 12 and 36 h.

3.2. X-ray diffraction

Fig. 3 shows X-ray diffraction patterns recorded at room temperature on samples sintered at 750°C,

Table 1
Relative densities as a function of sintering temperature in $Bi_{26}Mo_9WO_{69}$

Sintering temperature (°C)	Sintering time (h)	Relative density (%)[a]
750	0.2	91.5 ± 0.7
750	1	96.4 ± 0.3
800	1	96.7 ± 0.1
850	1	96.7 ± 0.7
900	1	96.4 ± 0.6
900	12	96.2 ± 0.6
900	36	95.7 ± 0.2

[a] Theoretical density = 7.63 g/cm^3 [4].

850°C and 900°C for 1 h. Specimens sintered at 850°C and 900°C show the characteristic doublet at $2\theta = 27°$ due to triclinic distortion. This doublet is not observed in the specimen sintered at 750°C. In this case, the Bragg peaks have larger width because of the smaller crystallite size, and the resolution is lowered.

Fig. 4 shows high-temperature X-ray diffraction patterns of samples sintered at 750°C and 900°C for 1 h.

The triclinic–monoclinic phase transition on heating and its reversibility on cooling are clearly observed around 260°C for both samples. However, for the sample sintered at 750°C (grain size of about 1 μm), this phase transition begins at 200°C and both structural phases coexist between 200°C and 260°C. For samples sintered at 900°C (grain size of about 10

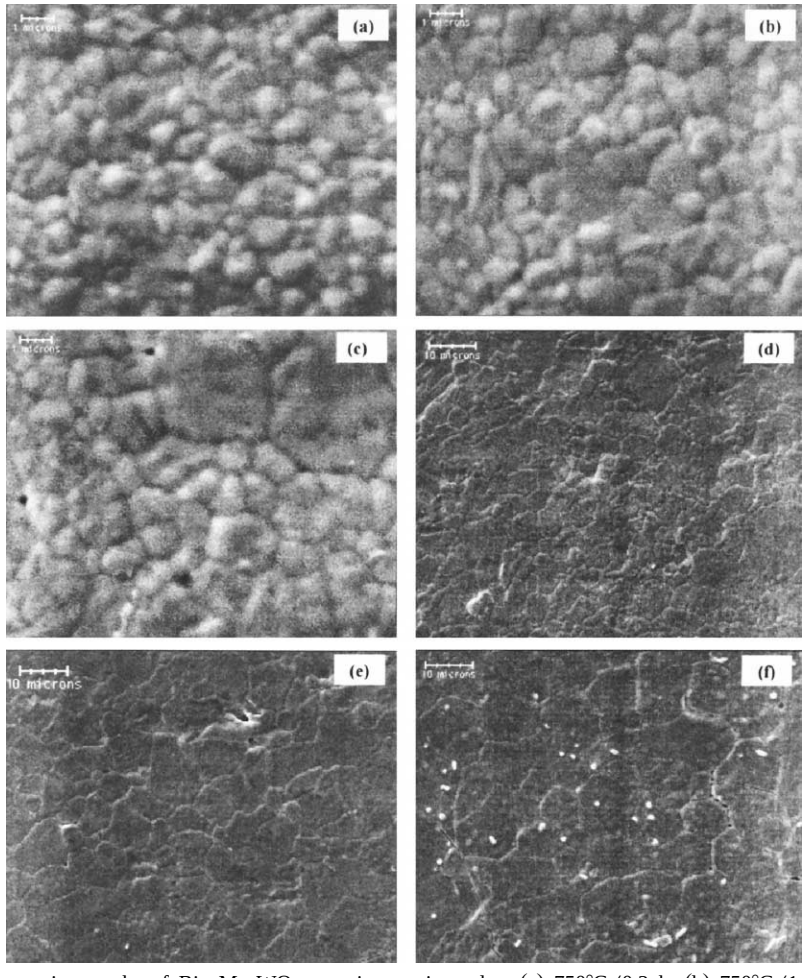

Fig. 2. Scanning electron micrographs of $Bi_{26}Mo_9WO_{69}$ specimens sintered at (a) 750°C/0.2 h, (b) 750°C/1 h, (c) 800°C/1 h, (d) 850°C/1 h, (e) 900°C/1 h and (f) 900°C/36 h.

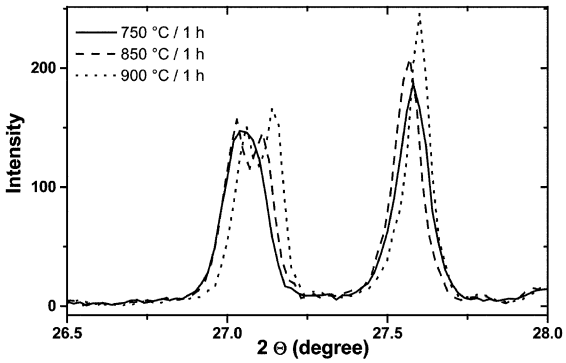

Fig. 3. X-ray diffraction patterns of $Bi_{26}Mo_9WO_{69}$ specimens sintered at 750°C, 850°C and 900°C for 1 h.

μm) the phase transition occurs rapidly around 260°C without any coexistence of two phases. This result is the first evidence of the grain size influence on the phase transition of $Bi_{26}Mo_9WO_{69}$.

3.3. Impedance spectroscopy

3.3.1. Impedance diagrams as a function of the applied signal

To separate out the electrolyte and the electrode contribution of the impedance diagrams, three signal amplitudes were used in impedance measurements: 100 mV, 500 mV and 1 V. Fig. 5 shows impedance diagrams at 280°C of samples sintered at 750°C/1 h and 900°C/12 h as a function of the applied signal. Only the low frequency region, between 1 and 0.1 Hz, is affected by changing the amplitude of the applied signal. The estimated capacitance values for the response in this low frequency region are close to 10^{-5} F. These are indications that the low frequency regions of the impedance diagrams are the response of the electrolyte/electrode interface. In this study the electrode responses in the impedance diagrams were subtracted.

The range switching of the Solartron 1260 between 5 kΩ and 50 Ω feedback resistor is visible at 1 MHz in the impedance diagrams for a specific resistance range (in the region of 5 kΩ). Some scattering of experimental data are observed at high frequencies, especially in the same range of resistance values that occurs the switching of the feedback resistor. It is worthwhile to point out that this scattering is more evident for data points at frequencies above 10 MHz, which were not taken into account in the fitting of the diagrams.

3.3.2. Influence of the thermal history on the impedance diagrams

Impedance measurements were performed during heating in three consecutive heating/cooling cycles between 200°C and 500°C in air. The first heating was from room temperature up to 320°C, followed by cooling to 220°C; after 12 h at that temperature, the temperature is increased up to 350°C, followed by cooling to room temperature; after 48 h at that temperature, the temperature is increased up to 500°C. Fig. 6 shows impedance diagrams measured at 226°C (before phase transition) and 322°C (after phase transition) for the three different heating profiles, for samples sintered at 750°C/1 h and 900°C/12 h. At 322°C, in the monoclinic domain, the impedance diagrams of samples sintered at the same temperature are similar indicating that the electrical properties do not depend on the thermal history for temperatures above the phase transition (the dependence of sintering temperature on the impedance diagrams is discussed in next section). At 226°C (triclinic domain), on the other hand, the impedance diagram after the second heating profile shows that $Bi_{26}Mo_9WO_{69}$ retains a portion of the high conductivity monoclinic phase. Impedance spectroscopy measurements during the third heating profile show that the samples are less resistive than during the first heating. Total resistivities during the second heating (third heating) for the sample sintered at 750°C/1 h and 900°C/1 h are 26% (66%) and 28% (88%) of the total resistivity during the first heating, respectively. That difference indicates that specimens sintered at 750°C (smaller grain sizes) have slower kinetic for phase transition than those sintered at 900°C. From these observations, we can conclude that the electrical properties and the phase transition in $Bi_{26}Mo_9WO_{69}$ ceramics depend on thermal history and grain size. In order to get more details on the electrical and structural properties, the same thermal cycle was applied to all specimens sintered at different temperatures. The impedance spectroscopy analyses reported in this study are those of the third heating unless otherwise mentioned.

In order to investigate the phase transition dependence on the grain size, samples sintered at 750°C,

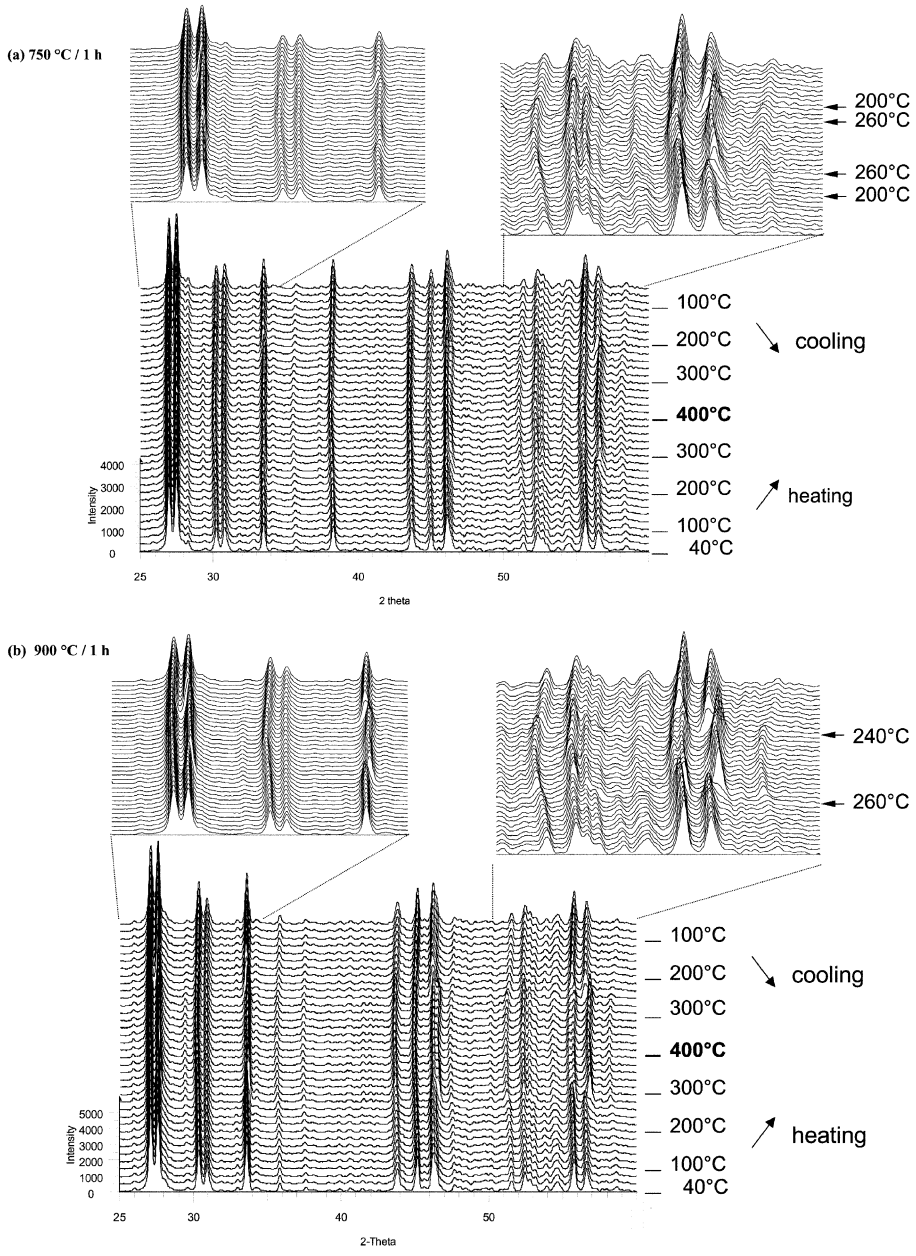

Fig. 4. High temperature X-ray diffraction patterns of $Bi_{26}Mo_9WO_{69}$ specimens sintered at (a) 750°C/1 h and (b) 900°C/1 h.

850°C and 900°C for 1 h were heated to 400°C for 2 h, and cooled down to 250°C. The impedance spectroscopy measurements were carried out as a function of time at 250°C. Fig. 7 shows the evolution of the total electrical resistivity (normalized to $t = 1$ h) as a function of time. It can be observed that the evolution of the total electrical resistivity depends on the grain size. Samples with smaller grain sizes have a slower evolution than samples with larger grain sizes.

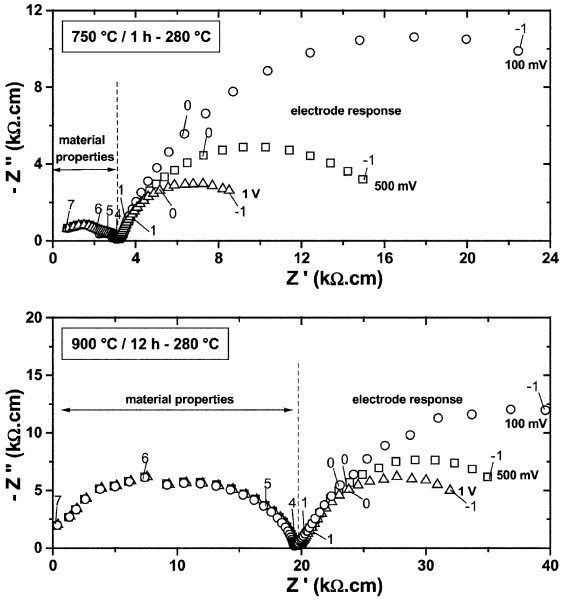

Fig. 5. Impedance diagrams for different amplitudes of applied signal of $Bi_{26}Mo_9WO_{69}$ specimens sintered at 750°C/1 h and 900°C/12 h measured at 280°C. In this figure and in Figs. 6, 8 and 11, the numbers indicate the logarithm of signal frequency.

3.3.3. Influence of the sintering temperature on the impedance diagrams

Fig. 8 shows the impedance diagrams measured at several temperatures of samples sintered at different temperatures. An evolution of the shape of the impedance diagrams can be observed as a function of the measuring temperature (in the phase transition temperature range) and sintering conditions. It is characterized by two main features: the decrease of the total electrical resistivity and a progressive distortion towards a two-semicircle shape.

Several conclusions can be drawn from the diagrams. At low temperatures (Fig. 8a), all samples show only one semicircle with calculated capacitance values around 8×10^{-12} F. An increase of the total resistivity with sintering temperature and time (which is directly related to the microstructure evolution shown in Fig. 2): 95 and 750 $k\Omega \cdot cm$ for samples sintered at 750°C/0.2 h and 900°C/36 h, respectively.

Specimens sintered at 750°C are less resistive before phase transition ($T < 300$°C). Samples sintered at temperatures higher than 750°C show a rapid decrease of the total electrical resistivity, that starts at approximately 260°C. This decrease is observed to happen at lower temperatures for samples sintered at 800°C and 850°C (with intermediary grain sizes) than in samples sintered at 900°C (Fig. 8b and c). After phase transition the samples sintered at 750°C have larger resistivities than all sintered at higher temperatures (Fig. 8d). Specimens sintered at 750°C clearly exhibit two semicircles for temperatures higher than approximately 260°C that are most probably related to the intragranular properties and intergranular blocking of charge carriers, since they have the higher grain boundary density (smaller grain size) [17–19]. All specimens sintered at 800°C and higher temperatures show highly distorted semicircles during the phase transition (Fig. 8c) and two semicircles are identified for temperatures above the phase transition (Fig. 8d). Because of the high conductivity and the consequent inductive parasite effect of the experimental setup, it was not possible to resolve the diagrams for temperatures above 280°C, except for samples sintered at 750°C and measured between 260°C and 310°C (Fig. 11).

In the triclinic domain only one semicircle was observed. A possible interpretation is that the triclinic, monoclinic and the grain boundary contributions overlap, with the triclinic response in the middle. After the phase transition, the triclinic response vanishes and it is possible to separate out the monoclinic bulk and grain boundary relaxations.

3.3.4. Impedance spectroscopy analysis

Fig. 9 shows Arrhenius plots of the total electrical conductivities of the studied samples. Three domains are evidenced: monoclinic, phase transition and triclinic ranges. The phase transition is clearly observed around 280°C. Two distinct groups can be distinguished: specimens sintered at 750°C and specimens sintered at higher temperatures. The specimens sintered at 750°C exhibit a continuous transition of the electrical conductivity values close to the phase transition temperature. The specimens sintered at higher temperatures are less conductive at temperatures below 280°C and the electrical conductivity values increase rapidly in the 260–280°C range. For temperatures above 300°C, the electrical conductivity values are of the same order of magnitude for all sintering temperatures. The average activation en-

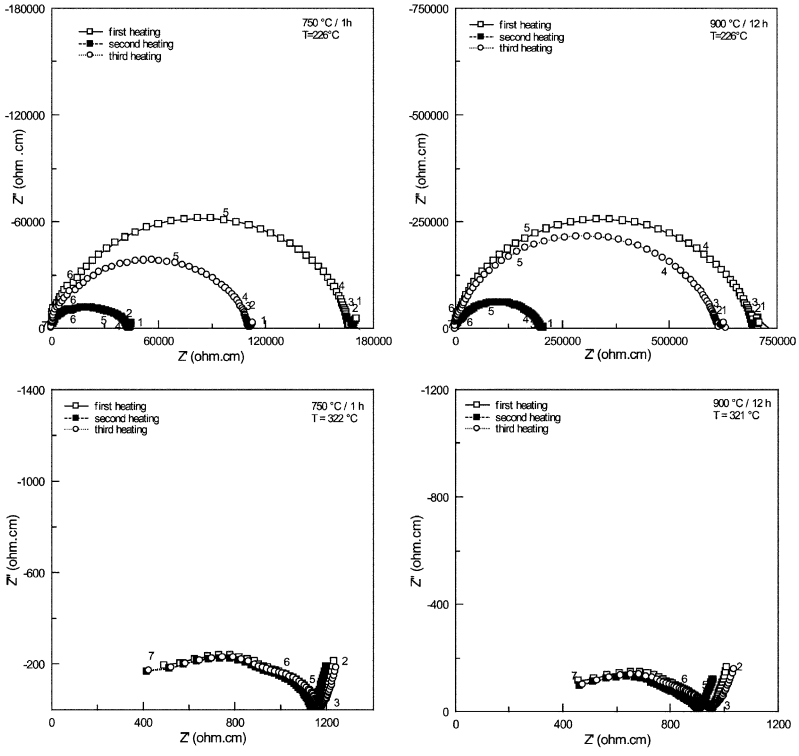

Fig. 6. Impedance diagrams of $Bi_{26}Mo_9WO_{69}$ specimens sintered at 750°C/1 h and 900°C/12 h measured at 226°C and 322°C for the three different heating cycles.

ergy values calculated for the triclinic and monoclinic phases, taking into account all sintering temperatures, are 1.1 ± 0.1 eV and 0.48 ± 0.04, respectively.

Fig. 10 shows the depression angle (β) values as a function of temperature. Samples sintered at 750°C/1 h, 800°C/1 h and 850°C/1 h have similar values, approximately 13°, at low temperatures. This is a value usually obtained for fitted bulk semicircles in impedance diagrams [11,20]. The samples sintered at 750°C/0.2 h and at 900°C have higher values of β probably related to the lower homogeneity of these samples due to the presence of pores and cracks [20,21], respectively. The depression angle is presented in this study as a representation of the one-towards-two semicircles shape distortion with increasing temperature and its dependence on grain size. Samples sintered at 750°C display a continuous increase of β, and for 240°C the β values are around 30°. Samples sintered at higher temperatures initially have constant β values and exhibit a rapid increase with increasing temperature. This rapid increase of β values starts at 250°C for samples sintered at 800°C and 850°C and, at approximately 270°C for samples sintered at 900°C. For β values exceeding 30°, it was difficult to resolve the impedance diagrams using a one-semicircle model. The

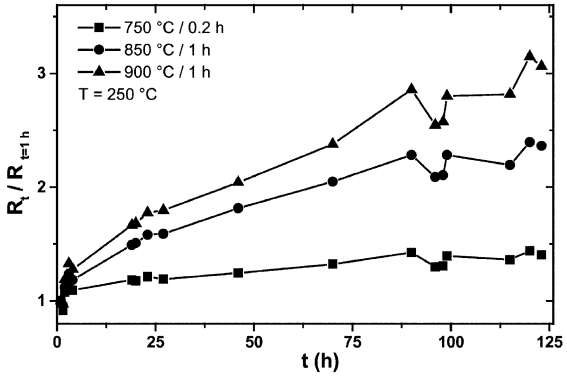

Fig. 7. Isothermal evolution of the total electrical resistance.

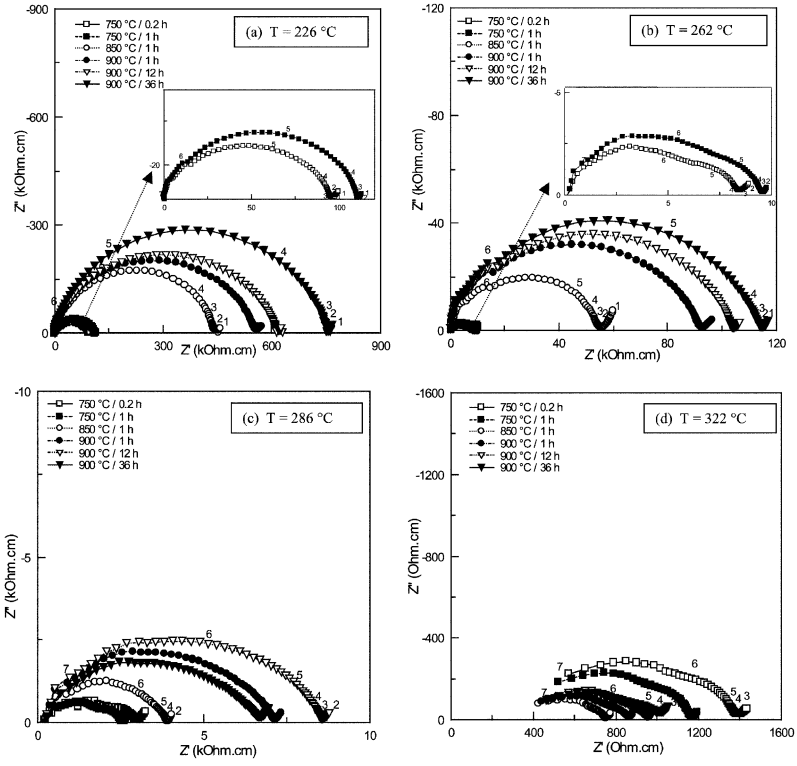

Fig. 8. Impedance diagrams of $Bi_{26}Mo_9WO_{69}$ specimens measured at 226°C, 262°C, 286°C and 322°C.

divergence of the depression angle is related to the splitting of the impedance diagrams into a two semicircles shape and characterizes the triclinic-to-monoclinic phase transition.

Impedance diagrams of samples sintered at 750°C were resolved using a two-semicircles model for temperatures between 260°C and 310°C. An example is shown in Fig. 11. The capacitance values for the

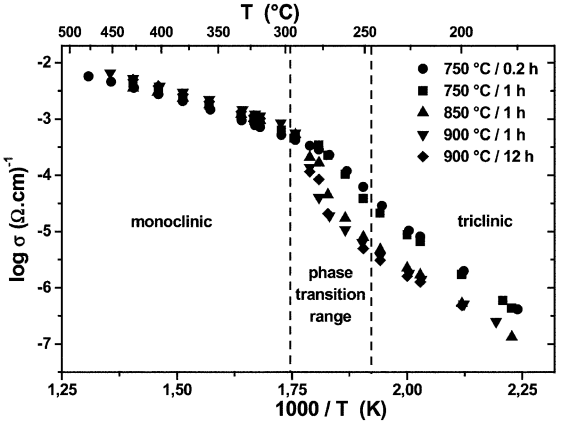

Fig. 9. Arrhenius plots of the total electrical conductivity determined from the impedance diagram of $Bi_{26}Mo_9WO_{69}$ samples.

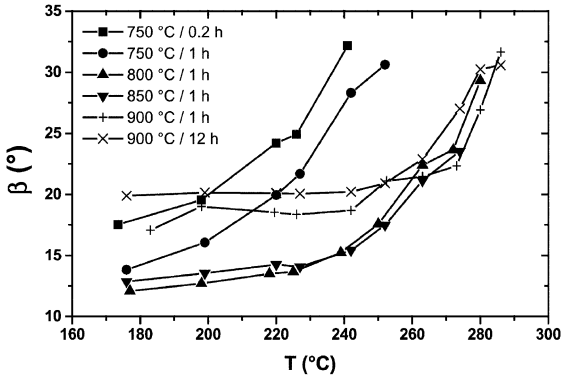

Fig. 10. Dependence of the depression angle values on the temperature of measurement of the impedance diagrams of $Bi_{26}Mo_9WO_{69}$.

HF semicircle and LF semicircle are around 10^{-11} and 10^{-9} F, respectively. These values are within the accepted range for capacitance values corresponding to bulk and grain boundaries [22] and are related to the monoclinic bulk and grain boundary relaxations, respectively.

In addition to the electrical conductivity, another parameter derived from the fitting of the impedance diagram can be used to describe the phase transition and the splitting of the impedance diagrams before phase transition (one semicircle) and after (two semicircles). This parameter is the relaxation frequency (the apex frequency of a semicircle) and its major advantage in relation to the electrical conductivity is that this parameter does not depend on sample's geometry [23]. Fig. 12 shows the Arrhenius plot of the relaxation frequencies.

For low temperatures ($T < 250$°C; triclinic domain), specimens sintered at 750°C have larger relaxation frequency values than samples sintered at higher temperatures. For temperatures between 260°C and 310°C, samples sintered at 750°C have higher relaxation frequency values for the HF semicircle (related to monoclinic relaxation) than would be expected by the linear fitting of the relaxation frequencies at temperatures below 250°C (triclinic domain). Since triclinic phase and grain boundaries (LF semicircle) have very close values of relaxation frequency, the two contributions are very convoluted at low temperatures and could not be separated.

The higher values of the relaxation frequency and electrical conductivity at low temperatures ($T <$ 250°C) for samples sintered at 750°C (grain size ≤ 1 μm), in comparison with samples sintered at higher temperatures, can be explained by the presence of some content of monoclinic phase at temperatures as low as 180°C.

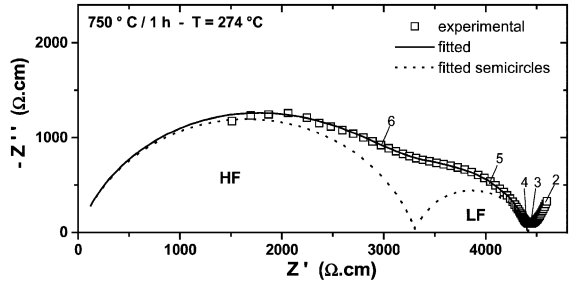

Fig. 11. Impedance diagrams of $Bi_{26}Mo_9WO_{69}$ sintered at 750°C/1 h, measured at 274°C. The fitted impedance diagrams are also shown.

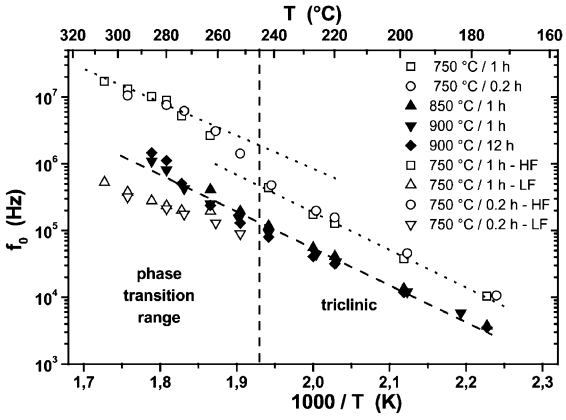

Fig. 12. Arrhenius plots of the relaxation frequency determined from the impedance diagrams of $Bi_{26}Mo_9WO_{69}$. The linear fitting of the data is also shown.

4. Conclusions

Using reactive $Bi_{26}Mo_9WO_{69}$ ceramic powders, prepared by solid state reaction and attrition milling, specimens were obtained by sintering at relatively low temperature (750°C) with relative density up to 96% of the theoretical density. Specimens with different average grain sizes were produced by varying sintering temperature and time. In the high-temperature monoclinic domain, the dependence of the impedance spectroscopy results on the microstructure is negligible. However, in the low temperature triclinic domain, the electrical properties and the kinetics of the transition are clearly dependent upon the microstructure: specimens with small grain sizes keep the monoclinic phase down to temperatures lower than those with relatively larger grain sizes. The impedance spectroscopy results regarding the phase transition dependence on grain size are in good agreement with the X-ray diffraction results. Hence, the results presented here confirm that the impedance spectroscopy technique is a useful tool to study phase transitions in ceramic solid electrolytes,

provided the phases involved have different electrical resistivities [13].

Acknowledgements

The authors gratefully acknowledge F. Ratajczak for powder preparation. One of the authors (F.C.F.) acknowledges FAPESP (Project 97/00727-3) for supporting his stay in France.

References

[1] T. Takahashi, H. Iwahara, Y. Nagai, J. Electrochem. Soc. 117 (1970) 244.
[2] F. Abraham, J.C. Boivin, G. Mairesse, G. Nowogrocki, Solid State Ionics 40–41 (1990) 934.
[3] R.N. Vanier, G. Mairesse, F. Abraham, G. Nowogrocki, J. Solid State Chem. 122 (1996) 394.
[4] R.N. Vanier, S. Danzé, G. Nowogrocki, Mairesse G. Huvé, Solid State Ionics 136–137 (2000) 51.
[5] B. Steele, C. R. Acad. Sci. Paris 1 (IIc) (1998) 533.
[6] E.C. Subbarao, in: A.H. Heuer, L.W. Hobbs (Eds.), Advances in Ceramics, Science and Technology of Zirconia, vol. 3, The American Ceramic Society, Columbus, OH, USA, 1981, 1.
[7] R.C. Garvie, J. Phys. Chem. 69 (4) (1965) 1238.
[8] R.C. Garvie, J. Phys. Chem. 82 (2) (1978) 218.
[9] J. Bauerle, J. Phys. Chem. Solids 30 (1969) 2657.
[10] S.P.S. Badwal, Solid State Ionics 76 (1995) 67.
[11] M.C. Steil, F. Thevenot, M. Kleitz, J. Electrochem. Soc. 144 (1997) 390.
[12] D.Z. de Florio, R. Muccillo, Solid State Ionics 123 (1999) 301.
[13] E.N.S. Muccillo, M. Kleitz, J. Eur. Ceram. Soc. 16 (1996) 453.
[14] M.C. Steil, J. Fouletier, M. Kleitz, P. Labrune, J. Eur. Ceram. Soc. 19 (1999) 815.
[15] J. Fleig, J. Maier, Phys. Chem. Chem. Phys. 1 (1999) 3315.
[16] K. Huang, M. Feng, J.B. Goodenough, J. Am. Ceram. Soc. 79 (4) (1996) 1100.
[17] A.I. Ioffe, M.V. Inozemtzev, A.S. Lipilin, M.V. Perfilev, S.V. Karpachov, Phys. Status Solidi A 30 (1975) 87.
[18] S.H. Chu, M.A. Seitz, J. Solid State Chem. 23 (1978) 287.
[19] M.J. Verkerk, B.J. Middelhuis, A.J. Burggraaf, Solid State Ionics 6 (1982) 159.
[20] L. Dessemond, PhD Thesis, INPG, Grenoble, France, 1992.
[21] L. Dessemond, M. Kleitz, J. Eur. Ceram. Soc. 9 (1992) 35.
[22] J.G. Fletcher, A.R. West, J.T.S. Irvine, J. Electrochem. Soc. 142 (8) (1995) 2650.
[23] M. Kleitz, H. Benard, E. Fernandez, E. Schouler, in: A.H. Heuer, L.W. Hobbs (Eds.), Advances in Ceramics, Science and Technology of Zirconia, vol. 3, The American Ceramic Society, Columbus, OH, USA, 1981, 310.